PAPER • OPEN ACCESS

3D numerical study of neutral gas dynamics in the DTT particle exhaust using the DSMC method

To cite this article: C. Tantos *et al* 2024 *Nucl. Fusion* **64** 016019

OPEN ACCESS
IOP Publishing | International Atomic Energy Agency
Nuclear Fusion
Nucl. Fusion **64** (2024) 016019 (20pp)
https://doi.org/10.1088/1741-4326/ad0c80

3D numerical study of neutral gas dynamics in the DTT particle exhaust using the DSMC method

C. Tantos[1,*], S. Varoutis[1], V. Hauer[1], C. Day[1] and P. Innocente[2]

[1] Karlsruhe Institute of Technology, Hermann-von-Helmholtz-Platz 1, 76344 Eggenstein-Leopoldshafen, Germany
[2] Consorzio RFX, Corso Stati Uniti 4, 35127 Padova, Italy

E-mail: christos.tantos@kit.edu

Received 20 July 2023, revised 30 October 2023
Accepted for publication 14 November 2023
Published 24 November 2023

Abstract

Recently the design of the divertor tokamak test (DTT) Facility divertor has been modified and consolidated. The new divertor design presents significant geometrical differences compared to the previous ITER-like one, including the presence of a more flattened dome shape. This paper presents a complete 3D numerical analysis of the neutral gas dynamics inside the DTT subdivertor area for the latest divertor design. The analysis has been performed based on the direct simulation Monte Carlo method by applying the DIVGAS simulator code. SOLEDGE2D-EIRENE plasma simulations have been performed for a deuterium plasma scenario at the maximum additional power in partially detached condition achieved by neon impurity seeding and the extracted information about the neutral particles has been imposed as incoming boundary conditions. The pumping efficiency of the DTT divertor is examined by considering various cases with respect to the pumping probability and the effect of the toroidal and poloidal leakages is quantified. The results show that a significant percentage of the incoming flux of neutrals returns back to the plasma site through the entry gaps (60% for deuterium and 40% for neon), and, consequentially, only a small percentage (∼2%–15%) of the incoming flux can be pumped out from the system. The toroidal leakages affect significantly the pumping performance of the divertor causing a significant decrease in the pumped flux (and also in the pressure at the pumping opening) about 37%–47% and 43%–56% for deuterium and neon respectively. It is discussed how many pumping ports are needed depending on the achievable pumping performance per port. The number can be reduced by closing the toroidal gaps. The analysis shows that enlarging the poloidal gaps by a factor of two causes a significant increase in the poloidal flux losses by a factor 1.7. It is also illustrated how the presence of the cooling pipes leads to conductance losses.

Keywords: divertor tokamak test facility (DTT), vacuum pumping, DSMC method, particle exhaust, SolEdge2D-Eirene, pumped fluxes, neutral gas dynamics

(Some figures may appear in colour only in the online journal)

* Author to whom any correspondence should be addressed.

1. Introduction

The DTT facility has been charged with the challenge to test the science of tokamak alternative divertor concepts under integrated physics and technical conditions that can reliably be extrapolated to DEMO (DEMOnstration power plant). Divertor Tokamak Test (DTT) aims to conduct scale experiments to find divertor solutions that can be well integrated into the specific physical conditions and technological environment foreseen in the DEMO reactor [1, 2].

The divertor plays a fundamental role in the achievement of the performance requested for a fusion reactor. In general, in a fusion reactor the divertor design has to reconcile conflicting requirements coming from the main functionalities, namely neutron shielding, heat removal and particle exhaust. A thorough study of the divertor region is quite challenging mainly due to its usual geometrical complexity but also for the increased computational difficulties related to the significant effect of particle collisions on the neutral gas dynamics. In the divertor region, the neutral gas dynamics must be described by the Boltzmann equation, for which even today an analytical solution is impossible. The only numerical tool that can reproduce accurately and reliably the solution of the Boltzmann equation is the Direct Simulation Monte Carlo (DSMC) method proposed by Bird in 1963 [3, 4]. Wagner in 1992 [5] proved that the DSMC method solution is equivalent to solving the Boltzmann equation itself for an adequate large number of neutral gas particles. At the Karlsruhe Institute of Technology in Germany, a DSMC numerical code, namely the DIVertor GAs Simulator (DIVGAS), has been developed, aiming to simulate 2D/3D multispecies gas flows inside the divertor region of fusion devices (i.e. tokamaks and stellarators). The code has been already applied to study particle exhaust in various fusion machines, such as the JT-60SA [6], JET subdivertor [7, 8] and DEMO [9, 10]. Recently in [11], the neutral gas dynamics inside the DTT divertor has been analyzed using the DIVGAS numerical tool. More specifically, using a simplified 2D model for an ITER-like divertor, a first assessment of the DTT divertor pumping performance was made assuming various plasma puffing and pumping scenarios. Based on the outcome of this work and also the design constraints, the position and size of the pumping opening was determined. In 2022, the DTT divertor design changed significantly and it is questionable whether the previous conclusions made for previous designs hold true for the new design. At the same time, the new design is considered now stable and consolidated and no major design modifications are expected in the near future.

Based on all of the above, it is evident that a thorough investigation of the new divertor design is necessary. Hence, in the present work the neutral gas flow in the sub-divertor area of DTT is studied performing 3D simulations. The simulation model is characterized by high geometrical complexity and represents accurately the given divertor design. Various scenarios with varied attached pumping speed are considered and the effect of the toroidal and poloidal leakages is investigated in a very detailed manner. The corresponding SolEdge2D-EIRENE plasma simulations have been performed and the incoming boundary conditions between the plasma and divertor sites are defined consistently. The obtained numerical results provide a very comprehensive information about the gas flow field in the sub-divertor area and can further support the ongoing design of the DTT particle exhaust system.

The paper is structured as follows: In section 2, the DTT divertor simulation model is presented and a detailed description of the various applied boundary conditions is provided. In addition, section 2 describes the definition of the boundary conditions at the entry gaps of the subdivertor region using the SolEdge2D-EIRENE data. Next, in section 3 a brief summary of the implemented DSMC numerical approach is given and all the values of the numerical parameters are defined. In section 4, the numerical results are presented and discussed in detail. Finally, section 5 presents a summary of the present work and the main findings are pointed out.

2. 3D DTT divertor simulation model and boundary conditions

The complete simulation model applied in this work is shown in figure 1 and constitutes a faithful representation, based on the most recent design, of about half of a 20° sector out of the 18 sectors in total that form the entire DTT divertor ring. As it can be seen in figure 1, the inner surface of the vacuum vessel along with the back surfaces of the divertor targets and the flattened dome, form the outer wall surfaces of the 10.8° simulation model. The poloidal gaps between the divertor cassettes (black surfaces) as well as the toroidal gaps between the targets and the vacuum vessel (red surfaces) are included in the present model and extended analysis of their effect on the divertor pumping efficiency is performed in this work. In addition, the model includes a detailed representation of the internal structures, namely the toroidal magnetic coils, the divertor cassette as well as the cooling pipes. The bottom view of the model, shown in figure 1, illustrates the shape of the pumping opening with a total area of 0.151 m^2, which leads through the pumping ducts to the actual pumps (both ducts and pumps are not shown in figure 1). Note that not all 18 pumping openings of the divertor ring (one pumping opening per sector) will be available for pumping and based on the current pumping design status, the desired number of pumping openings is 9–10. It should be noted that the choice of the present model was made taking into account that it allows a systematic study of the effect of various three-dimensional geometrical effects.

In the present 3D simulation model, the neutral particles enter the domain through the inner (light blue surfaces) and the outer (dark blue surfaces) entry gaps. Since the neutral-neutral collisions are taken into account, the neutrals can interact with each other as well as with the surrounding solid walls (i.e. back surface of the targets and the dome, inner surface of the vacuum vessel, magnetic coils, walls of the divertor cassette and the external walls of the cooling pipes) of the simulation domain. When the neutrals interact with the open gaps (poloidal and toroidal), the particles are completely

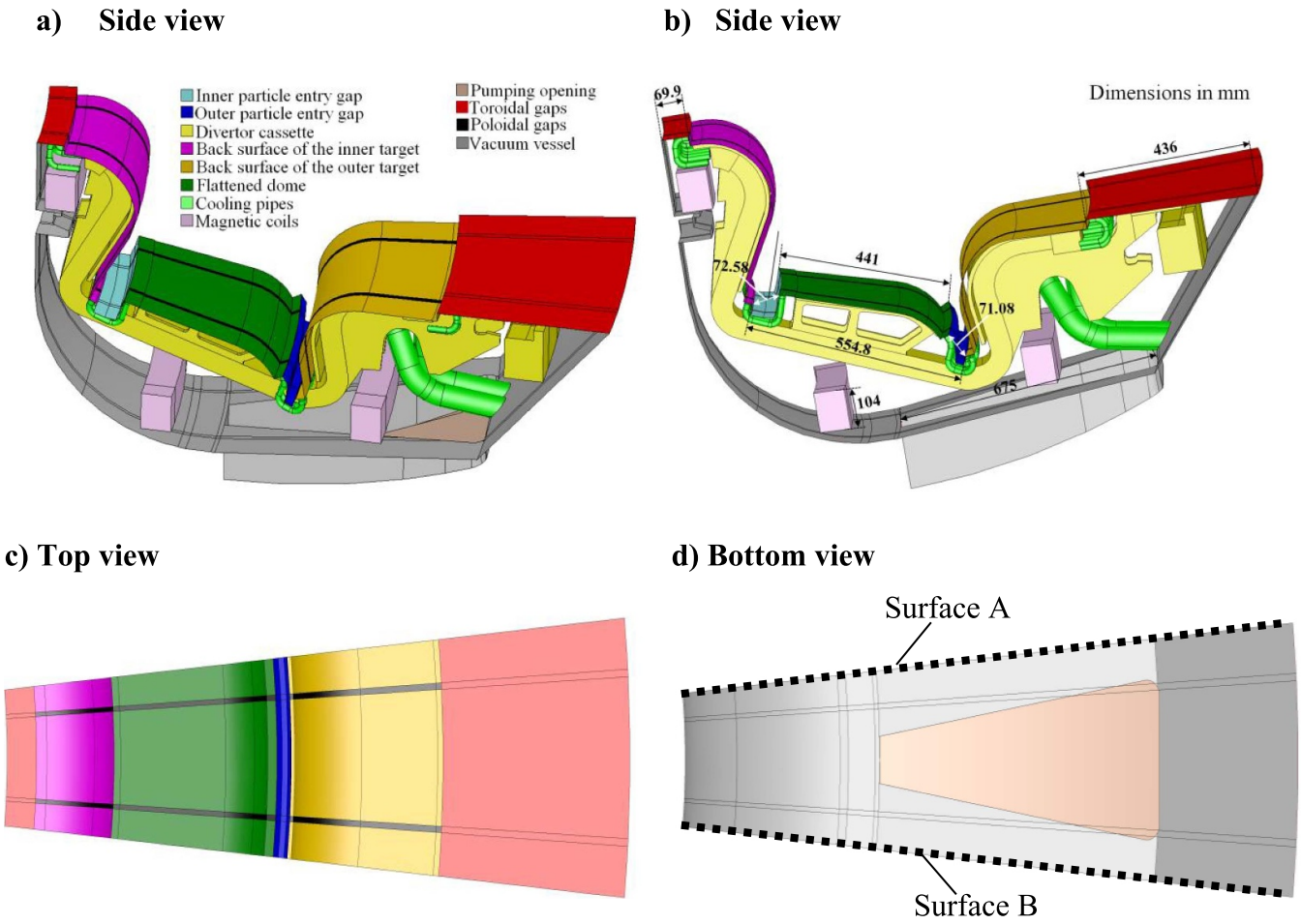

Figure 1. Different views of the simulated 10.8° DTT divertor model.

removed, thereby forming the corresponding poloidal and toroidal neutral fluxes through the leakages. It is also possible some particles to pass through the inner and the outer entry gaps towards the plasma core creating the inner and outer outfluxes respectively. The pumping process across the pumping opening is performed as follows: assuming a given pumping probability $0.05 \leqslant \xi \leqslant 0.3$ (i.e. the probability of a neutral to be pumped) the neutrals can be pumped from the pumping opening. In this sense, the pumping opening may be considered essentially as a solid absorption surface, assuming that particles hitting the openings are absorbed with a probability ξ or can be reflected diffusely backwards to the divertor volume with probability $1-\xi$ based on an isotropic Maxwellian distribution. It should be pointed out that the selected range for the pumping probability represents the range that can be provided by the cryogenic pump solution which has been decided to be used in DTT. At the side surfaces A and B (see bottom view in figure 1), the particles are specularly reflected back into the simulation domain to mimic their toroidal motion. Previous 3D DEMO divertor simulations [9] showed that such a choice describes effectively the toroidal symmetry conditions imposed on these two side surfaces. The temperature of the inner surface of the vacuum vessel, the magnetic coils, the walls of the divertor cassette and the external walls of the cooling pipes are kept at 343 K, while the back surfaces of the targets and the dome are kept at 353 K. Furthermore, in the present work the wall recombination of atomic deuterium to molecular deuterium has been included, which is considered to be the prevailing reaction at the expected temperatures. Within this gas-surface interaction process, deuterium atoms when impacting the wall are recombined to deuterium molecules based on a given recombination probability according to the provided database in [12] for tungsten. The rest of the deuterium atoms as well as neon particles are backscattered from the wall with a Maxwellian distribution function based on the wall temperature.

The imposed boundary conditions assume that a gas mixture consisting of molecular deuterium (D), and neon (Ne) enters the sub-divertor area through the inner and the outer entry gaps, based on the number density and temperature profiles provided by 2D SolEdge2D-EIRENE plasma simulations. Between the different plasma conditions studied with edge modeling, for the current analysis we have considered the most interesting scenario in terms of neutral dynamic which is the DTT operation at the maximum additional power ($P_{aux} = 45\ MW$) in partially detached condition achieved by

Table 1. SolEdge2D-Eirene overall fluxes to the inlet areas over the whole divertor ring Φ_{net} [s^{-1}], incoming fluxes to the inlet areas over the entire divertor ring $\Phi_{\text{in}}^{\text{DR}}$ [s^{-1}], and incoming particle fluxes Φ_{in} [s^{-1}] finally assumed in the present simulations at the inner and outer entry gaps of the model (see figure 2).

	Total overall flux across the entire divertor ring $\Phi_{\text{net}}^{\text{DR}}$ [s^{-1}]		Total incoming flux across the entire divertor ring $\Phi_{\text{in}}^{\text{DR}}$ [s^{-1}]		Incoming flux across the inlet areas Φ_{in} [s^{-1}]	
species	Inner entry gap	Outer entry gap	Inner entry gap	Outer entry gap	Inner entry gap	Outer entry gap
D	2.98×10^{22}	5.46×10^{22}	6.93×10^{23}	1.61×10^{24}	2.08×10^{22}	4.82×10^{22}
Ne	2.86×10^{20}	7.26×10^{20}	3.57×10^{21}	9.07×10^{21}	1.07×10^{20}	2.72×10^{20}

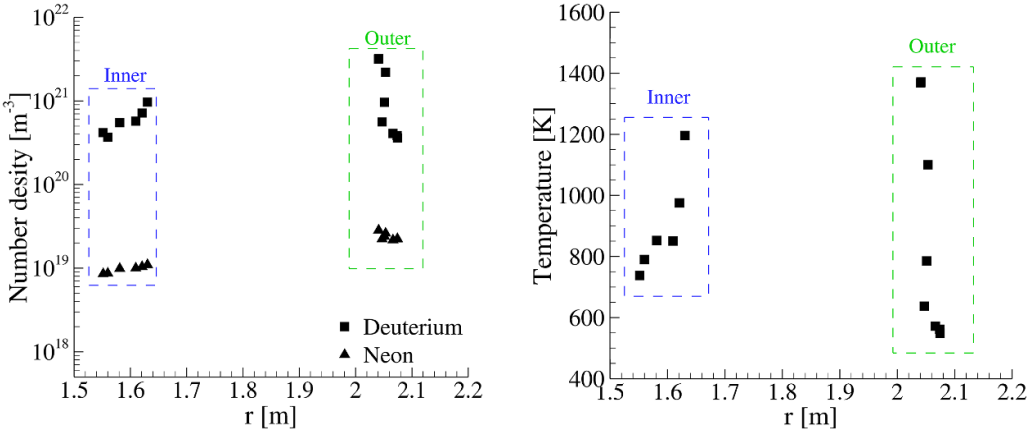

Figure 2. SolEdge2D-Eirene density and overall temperature profiles of neutrals at the inner and outer particle entry gaps.

neon impurity seeding. We have selected this scenario because the partially detached state provides stationary plasma operation compatible with the tungsten divertor and meanwhile it provides the highest pressures in the divertor region, which correspond also to the maximum throughput provided by the pumping system. The imposed puffing rate values for deuterium and neon were $\Gamma_{\text{D}} = 8.4 \times 10^{22}$ D s^{-1} and $\Gamma_{\text{Ne}} = 1 \times 10^{21}$ Ne s^{-1} respectively. It is noted that, in the SolEdge2D-EIRENE plasma simulations the subdivertor area is not included and the inner and the outer entry gap surfaces are modeled as pumping surfaces, with a given capture coefficient (albedo = 1-capture coefficient) namely 0.957 at the inner gap surface and 0.966 at the outer surface for deuterium and 0.92 for both surfaces for neon. Based on these albedo values, as shown in the second and third column of table 1, about 35% of the total deuterium puffing flux Γ_{D} escapes through the inner entry gap and 65% through the outer entry gap, with the corresponding percentages for neon being 28% and 72% respectively. In the DIVGAS simulations, the molecular deuterium (D), and neon (Ne) particles enter the domain according to the following flux (expressed in particles s^{-1}):

$$\Phi_{\text{in}} = \frac{An}{4}\sqrt{\frac{8k_{\text{B}}T}{\pi m}}, \tag{1}$$

where, A is the area of the inner and the outer entry gaps, k_{B} is the Boltzmann constant and m is the mass of the considered species. The temperatures T for each species in equation (1) were extracted from the SolEdge2D-EIRENE plasma simulation, while the number density n has been calculated numerically, in order the incoming fluxed Φ_{in} imposed in the DIVGAS simulations at the inner and the outer entry surfaces for each species to be equal to the corresponding SolEdge2D-EIRENE incoming flux of the same surfaces. The number density is considered to be uniformly distributed in the toroidal direction. The relation between the incoming fluxes to the entry surfaces (inner and outer) and the total overall flux, both expressed for the whole divertor ring, is defined as

$$\Phi_{\text{in}}^{\text{DR}} = \frac{\Phi_{\text{net}}^{\text{DR}}}{1 - \text{albedo}}, \tag{2}$$

and the obtained values of the partial incoming fluxes for the whole divertor ring are given in the fourth and fifth columns of the table 1. The final values of the incoming flux Φ_{in} for deuterium and neon across the inner and the outer entry gaps of the simulation model are deduced by normalizing the values of the total incoming flux $\Phi_{\text{in}}^{\text{DR}}$ according to the ratio of the corresponding areas, i.e. $A^{\text{Model}}_{\text{Inner/Outer gaps}}/A^{\text{DR}}_{\text{Inner/Outer gaps}} = 1/33$. The values of the incoming flux Φ_{in} are shown in the last two columns of table 1, while the corresponding poloidal density and the temperature distributions are shown in figure 2. It is noted that, the density points shown in figure 2, have been calculated so that the particle fluxes obtained from the Maxwellian distributions follow qualitatively and quantitatively the actual fluxes obtained as output from the SolEdge2D-EIRENE plasma simulations. The overall particle balance inside the sub-divertor regions can be expressed as follows:

$$\Phi_{\text{in}} = \Phi_{\text{pumped}} + \Phi_{\text{toroidal leakages}} + \Phi_{\text{poloidal leakages}} + \Phi_{\text{outflux}}, \tag{3}$$

where Φ_{pumped} is the flux through the pumping opening, $\Phi_{\text{toroidal leakages}}$ and Φ_{poloidal} leakages are the fluxes through the toroidal and poloidal leakages respectively, and $\Phi_{\text{outflux}} = \Phi_{\text{inner entry gap}} + \Phi_{\text{outer entry gap}}$ is the total flux of particles through the entry gaps towards the plasma site. In the particle flux balance equation (3), all the fluxes appearing on the right hand-side of the equation are unknown and obtained as part of the solution, while the particle flux Φ_{in}, as described above, is an input and is provided by the SolEdge2D-EIRENE simulations. In all simulations performed in the present work the equation (3) is fully satisfied.

3. Numerical method and numerical parameters

The only reliable mathematical tool for describing the neutral gas behaviour in the whole range of the gas collisionality, is the Boltzmann equation (BE). Nowadays, the most widespread and dominant method of solving the Boltzmann equation is the stochastic DSMC method [3]. In the DSMC method, the computational volume is discretised into computational volume elements, and the motion of the DSMC particles, which represent a larger number of the actual gas molecules, is tracked in time. At each discrete time step, two uncoupled steps take place, i.e. first the ballistic motion of the molecules in the physical space as well as the interaction with the solid walls and the open surfaces, and second the intermolecular collisions. The quantities of practical interest are calculated by sufficiently sampling the properties of the computational particles contained in each computational volume element. In the present work the collisions between the particles are modelled with the robust no-time-counter scheme (NTC), supplemented by the variable hard sphere (VHS) model [13]. The viscosity indexes of molecular deuterium (D_2), atomic deuterium (D) and neon (Ne) are taken equal to $\omega = 0.7$, 0.74 and 0.67 respectively in order for the VHS model viscosity to match the experimental viscosity values [14, 15] in a wide range of the gas temperature from 300 K to 2000 K with a maximum deviation of less than 3%. The model VHS molecular diameters of D, D_2, and Ne are taken equal to $d_{\text{D}} = 0.281$ nm, $d_{\text{D}_2} = 0.260$ nm and $d_{\text{Ne}} = 0.248$ nm respectively, in order that the VHS model reproduces the viscosity experimental data [14] at the reference temperature of 1000 K. The internal energy exchange during binary collisions of diatomic molecular deuterium among the gas mixture was modeled in accordance with the Borgnakke–Larsen phenomenological model [16]. The average number of particles in each simulation ranges between 300×10^6 and 500×10^6. The number of grid cells in all simulations is equal to 40×10^6. In all the present simulations, the time step $\Delta t = 0.1$ μs is chosen to be sufficiently smaller than the cell traversal time, defined as $\Delta x/u_0$ with u_0 being the most probable speed of the lighter particles and Δx is the cell size, in order to avoid light particles flying long distances. This number assures that the statistical scattering of macroscopic quantities along the computational domain is sufficiently low. In order to reduce the relative statistical scattering of the macroscopic quantities up to a value significantly smaller than the adopted uncertainty 5%, the macroscopic quantities have been obtained by time averaging over 9×10^6 time steps. The simulations of this work were performed on the MARCONI HPC and also partially on the HoreKa supercomputer using 4096 CPUs for each case (3–4 different values of ξ), and the typical time for reaching steady state conditions was approximately one week for each pumping probability ξ.

4. Results and discussion

In this section, the obtained numerical results are presented and discussed. The present three-dimensional computational geometry allows the systematic study of various 3D geometrical effects on the pumping performance of the DTT divertor. A very extensive parametric analysis is performed considering the following four cases:

- Case A: this case corresponds to the reference scenario, where the leakages through the toroidal and poloidal gaps as well as the presence of all cooling pipes are considered (see figure 1). Because of the flux losses through the open gaps low pumping efficiency is expected for this case, and it will be used as a reference point for examining the pumping performance of the other cases.
- Case B: in this case the effect of the toroidal gaps is investigated, by considering them completely closed. The only difference with the case A is that the interaction of the particles with the toroidal openings is modeled according to the gas-wall interaction model applied for all other solid walls of the divertor. Clearly this is an ideal case, which however demonstrates the maximum particle flux that can be achieved by completely eliminating particle losses from the toroidal gaps. In addition, the zero neutral gas flux through the toroidal gaps imposed at this case, makes it as close as possible to the SOLEDGE2D-EIRENE setup.
- Case C: in this case the effect of the size of the poloidal gaps (space between the divertor cassettes) on the pumping efficiency of the divertor is studied by increasing their average width by a factor of two, i.e. from 1 cm to 2 cm.
- Case D: in this case, the cooling pipes located underneath the inner and the outer entry gaps and between the flattened dome and the targets on the divertor have been completely removed in order to quantify the reduction in the divertor pumping capacity due to the presence of the cooling tubes. Hence, in contrast to case A, in case D the particles can enter the sub-deflector area without the neutral trajectories being blocked by the presence of the tubes.

For all the aforementioned cases, a wide range of values of the pumping probability, i.e. $0.05 \leqslant \xi \leqslant 0.3$, is studied highlighting the response of the pumping system in each case. Next, the results for the cases A, B, C, and D are categorized according to the various quantities of practical and theoretical interest.

4.1. Particle fluxes

In figure 3, all the particle fluxes appearing in the particle balance of the present 3D model for the case A, i.e. the pumped

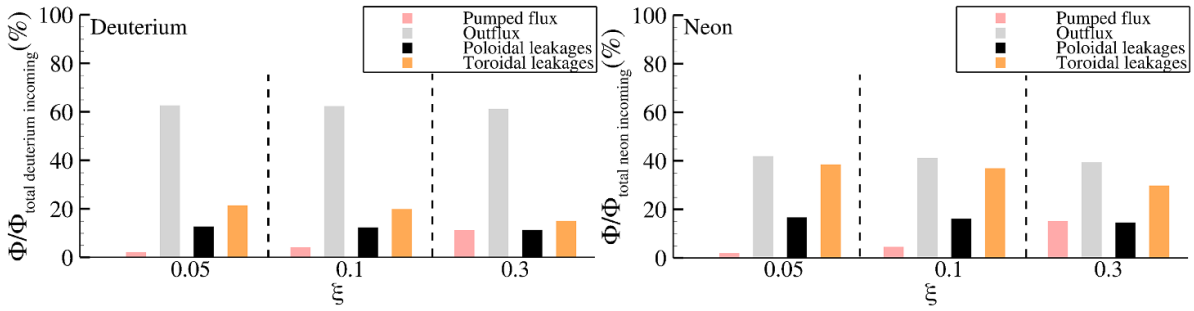

Figure 3. Various particle fluxes of deuterium (left) and neon (right) as percentage of the total incoming flux (inner + outer entry gaps) vs pumping probability ξ for the case A.

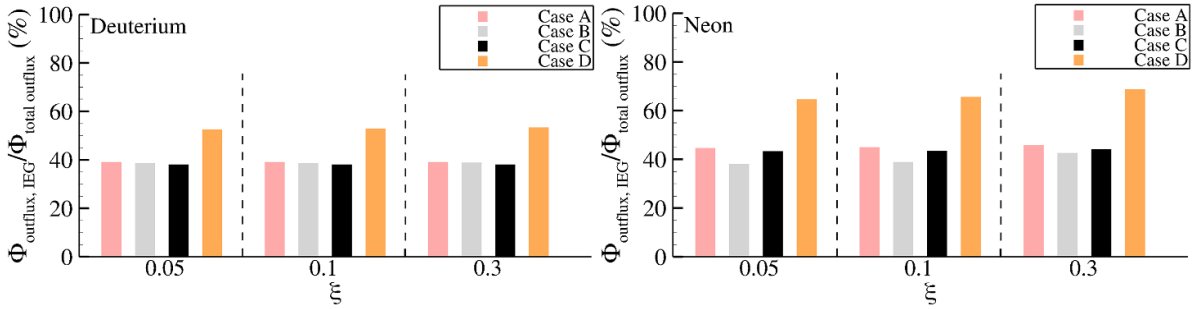

Figure 4. Percentage of the total outflux that passes through the inner entry gap (IEG) in the case of deuterium (left) and neon (right). The total outfluxes in the denominator represent the corresponding individual overall outfluxes of deuterium and neon.

flux, the outflow and the fluxes through the poloidal and toroidal leakages, are shown as a function of the pumping probability ξ. In all cases the corresponding partial particle fluxes are expressed as a percentage of the partial incoming flux. The partial fluxes of deuterium and neon are presented instead of the overall mixture fluxes (which can be easily obtained as the sum of the corresponding partial ones), since in that way a very detailed analysis on the divertor pumping capabilities for different components of the mixture is allowed. Note, that the partial incoming flux remains the same for all values of the pumping probability ξ and its values were derived from the SolEdge2D-EIRENE simulations as provided in the last two columns of table 1. It is seen that for all values of ξ, equation (1) is fully satisfied, highlighting the always present particle balance within the divertor volume. The results show that for both deuterium and neon, only a very small percentage of the incoming flux is pumped out of the system and this percentage for $0.05 \leqslant \xi \leqslant 0.3$ varies from 2% to 15 %. However, the total outflux remains always the highest percentage (about 60% for deuterium and 40% for neon) of the incoming flux and is slightly affected by the pumping probability ξ. However, despite the fact that the absolute differences with respect to ξ in the outflux remain small, the absolute numbers of the outflux are large, and for $\xi = 0.05$ and 0.3 the outflux values read as 4.37×10^{22} s^{-1}and 4.28×10^{22} s^{-1} for deuterium and 1.61×10^{20} s^{-1} and 1.52×10^{20} s^{-1} for neon respectively. As shown in figure 4, in case A about 40%–45% of this aforementioned high observed total outflux escapes through the inner inlet gap back to the plasma site and the rest escapes through the outer entry gap. This is justified by the fact that the incoming flux through the inner entry gap is essentially lower compared to that at the outer entry gap (see table 1). The results also indicate that particle flux losses through poloidal and toroidal leakages are very significant and for the case of deuterium and neon constitute 27%–35% and 45%–56% of the incoming flux, respectively.

Figure 5 illustrates the particle fluxes of case B as a function of ξ. In case B the toroidal gaps are treated by the particles as solid walls leading to zero flux through these surfaces. In order to better understand the effect of the toroidal leakages, the individual particle fluxes of case B are normalized to the corresponding ones of case A. It is observed that, by sealing the toroidal gaps the previously high particle flux losses through the toroidal gaps observed in case A, are distributed mainly to the pumping port and to the poloidal gaps, with the outflux slightly affected. The absence of toroidal leakages causes a significant increase in the pumped flux by a factor of 1.6–1.9 and 1.8–2.3 for deuterium and neon, respectively, while the losses through the poloidal leakages increase by a factor of 1.4–1.7 for deuterium and 1.7–1.9 for neon. These substantially high pumped fluxes that can be achieved in case B indicate the importance of eliminating the toroidal leakages as much as possible.

Next, the discussion on the particles fluxes continues in figure 6 presenting the data for case C. To facilitate comparison with the reference case A, the ratio $\Phi_{\text{Case C}}/\Phi_{\text{Case A}}$ is plotted as a function of ξ in the range $0.05 \leqslant \xi \leqslant 0.3$. The results show that widening the poloidal gaps by a factor of 2 causes a significant increase in the poloidal flux losses by a

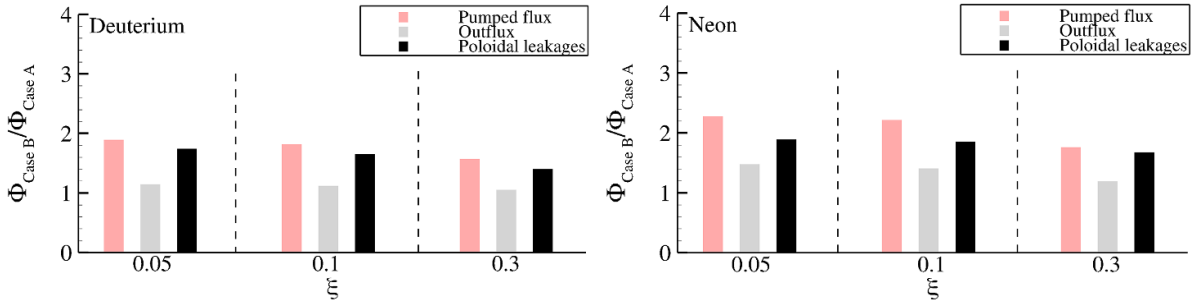

Figure 5. Various particle flux ratios $\Phi_{\text{Case B}}/\Phi_{\text{Case A}}$ as a function of the pumping probability ξ. The results for deuterium and neon are shown on the left and the right, respectively.

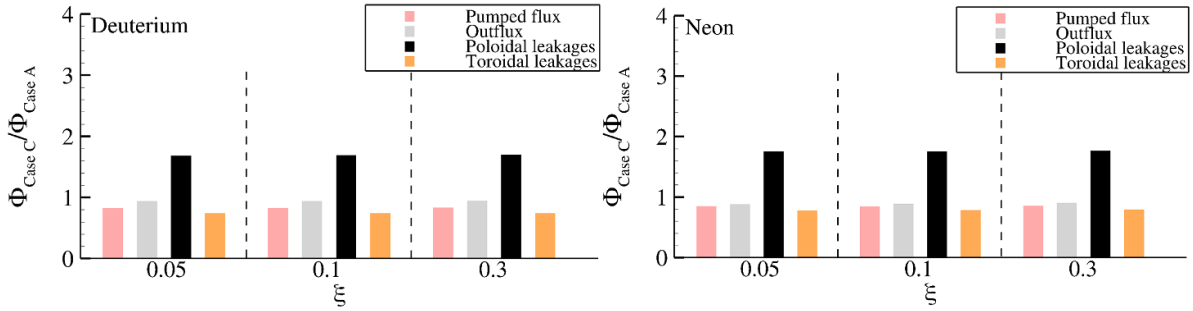

Figure 6. Various particle flux ratios $\Phi_{\text{Case C}}/\Phi_{\text{Case A}}$ as a function of the pumping probability ξ. The results for deuterium and neon are shown on the left and the right, respectively.

factor 1.7 with respect to that for case A. This implies that there is a strong, but less than linear, relationship between the poloidal gap width and the poloidal particle flux losses. In addition, in order to maintain the particle balance inside the subdivertor region, the mentioned increase in the poloidal gap width almost independently of the pumping probability leads to a decrease in the pumped flux, outflux and toroidal flux losses about 14%–16%, 4%–10% and 20%–25% respectively. It is noted that the aforementioned factors are only negligibly affected by the pumping probability ξ, and can be applied as a good approximation to both deuterium and neon.

From figures 3, 5 and 6, it can be seen that the outflux remains always the highest percentage of the incoming flux. It is obvious that one reason for the observed high outflux could be the presence of the cooling tubes at the subdivertor entry gaps which lead to additional backwards reflections of the incoming neutral particles. Thus, in figure 7, the particle fluxes of case D (without cooling pipes) are compared to the reference case A (with cooling pipes). The figure shows, that the cooling pipes increase the overall outflux through the entry gaps by a factor of about 1.3 and 1.5 in the case of deuterium and neon respectively. This numerical finding indicates that the high observed outflow (about 60%) of case A is not solely due to the presence of the cooling pipes at the entry gaps. It is clearly seen that the presence of the cooling pipes causes a decrease in the pumped flux about 24%–30%. It is also interesting that for case D, as it is shown in figure 4, in the case of deuterium the outflux is almost symmetrically distributed in the inner and the outer entry gaps, while in the case of neon, in contrast to the other examined cases A–C, the greater percentage (about 65%–69%) of the overall outflux passes through the inner entry gap.

4.2. *Pressure and temperature distributions*

In figure 8, the mixture pressure contours across the pumping opening are presented for various values of the pumping probability ξ as well as for all cases A–D. As it is clearly demonstrated, the pressure is not uniform along the pumping opening and in all examined cases and values of ξ, the highest values are observed on the inner side of the opening, while the pressure drops towards the outer side of the opening. It is observed that as ξ increases, the pressure over the whole pumping area decreases, due to the corresponding increase in the amount of particles that are pumped out through the pumping opening. By examining the differences between the different cases the following qualitative conclusions can be drawn: The highest pressure in the pumping opening is achieved by closing the toroidal leakages (Case B), the increase in the poloidal gap width (Case C) causes a small drop in the pressure at the pumping opening, and while the presence of the cooling pipes (Case A vs Case D) at the entry gaps reduces the pressure at the pumping opening. In order to have a quantitative assessment of the pressure differences between the various cases, figure 9 shows the average partial pressures of molecular deuterium, atomic deuterium and neon at the pumping opening for various values of ξ. In all cases the pressure of atomic deuterium is very small compared to that of molecular deuterium and this is justified by

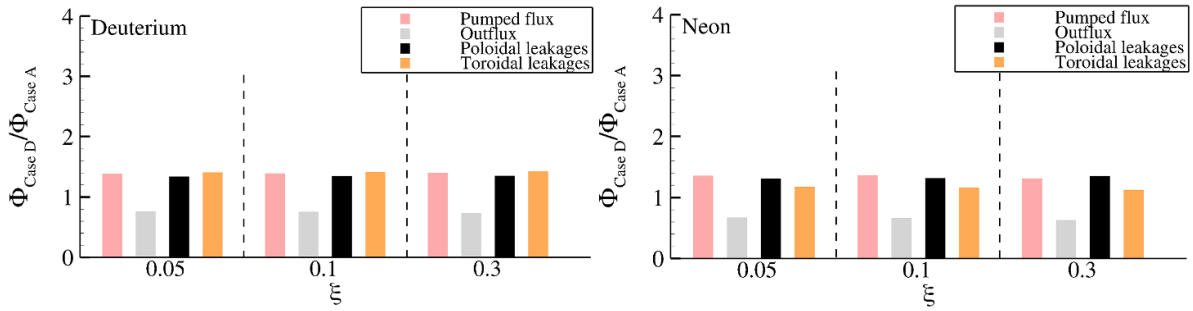

Figure 7. Various particle flux ratios $\Phi_{\text{Case D}}/\Phi_{\text{Case A}}$ as a function of the pumping probability ξ. The results for deuterium and neon are shown on the left and the right, respectively.

the intense formation of a large amount of incoming deuterium atoms into deuterium molecules due to the surface recombination process that takes place at the surrounding divertor solid walls. Furthermore, the neon pressure at the pumping opening is about two orders of magnitude smaller compared to that of molecular deuterium and one order of magnitude smaller compared to atomic deuterium. This pressure difference between neon and deuterium is in line with the large difference in the imposed incoming fluxes (about two orders of magnitude), as is easily seen in table 1. Depending on ξ, the overall deuterium pressure ranges between 2–3 Pa, 3–5.6 Pa, 1.7–2.4 Pa and 2.8–4 Pa for the cases A, B, C, and D, respectively, while the corresponding neon pressure ranges are 0.033–0.035 Pa, 0.061–0.076 Pa, 0.029–0.030 Pa, and 0.046–0.050 Pa. In figure 10, the corresponding mixture temperature contours are shown. In all cases, the temperature presents the same qualitative behaviour, namely high values at the central part of the pumping opening (353–395 K) and lower values (344–356 K) close to the walls. The temperature presents the opposite behaviour to that previously mentioned for pressure with respect to the pumping probability ξ, namely it increases as ξ increases. The reason is that as ξ increases a smaller number of particles is reflected back to the divertor volume from the pumping opening, preventing in this way the cooling of the incoming stream of the hotter molecules towards the pumping opening. It is also evident that the highest temperatures are observed for the case D, and this is explained by the fact that in absence of the cooling pipes at the entry gaps the neutrals particles enter the subdivertor hotter and eventually reach the pumping opening with a higher temperature compared to the cases A–C, in which a large amount of the hot incoming particles after colliding with the cooling pipes enter the subdivertor region at the temperature of the cooling pipes. Based on the pressure and temperature values shown in figures 9 and 10, the average Knudsen number, defined as $Kn = 1/\sqrt{2}nD_h\pi d_{\text{ref}}^2$ where $n = P/k_B\text{T}$ is the local mixture density, $d_{\text{ref}} = (d_{\text{D}_2} + d_{\text{D}} + d_{\text{Ne}})/3 = 0.263$ nm is the mean reference molecular diameter, and $D_{\text{h}} = 0.333$ m is the hydraulic diameter of the pumping opening, can be estimated. The average Knudsen number for the cases A, B, C, and D, is varying in the ranges 0.015–0.024, 0.008–0.015, 0.019–0.028 and 0.012–0.018, respectively. These values of the Knudsen number correspond to a neutral gas flow dominated by the neutral collisions which underlines the necessity to employ the full Boltzmann equation to describe the situation properly.

As such a parametric variation of 3D effects is not available in literature, the study of the pressure and temperature variation inside the sub-divertor is further deepened by presenting in figures 11–14 the pressure and temperature contours at three vertical cross-sections in the toroidal direction. The contours in figures 11 and 13 correspond to a weak pumping scenario ($\xi = 0.05$), while the contours figures 12 and 14 to a strong pumping scenario ($\xi = 0.3$), while for each one all the cases A-D are shown. In all the examined cases A–D, the change in pressure follows the same behaviour, i.e. increased values in the area between the divertor cassette and the flattened dome as well as in the area formed between the divertor cassette, the vacuum vessel and the magnetic coil, and then decreases as we approach the pumping opening. By comparing the pressure contours at different cross sections, it is also evident that the pressure variation in the toroidal direction is not very significant. Also, it is shown that the cases B and D are characterized by higher pressures (∼5.6–7.5 Pa is the maximum below the divertor cassette at $\xi = 0.05$) compared to the cases A and C (∼4.5–5.3 Pa is the maximum below the divertor cassette at $\xi = 0.05$). With respect to the effect of the pumping probability on the subdivertor pressure, it is seen that for the cases A, C and D, the increase in ξ causes a more pronounced pressure drop, mainly in the right part of the divertor and in the vicinity of the pumping opening, while for case B the pressure decreases more uniformly in the entire divertor volume. Regarding the temperature contours, it is clearly seen that for all cases A–D the neutral gas temperature remains high near the entry gap inlets and then reduces significantly below the divertor cassette and close to the pumping opening, where the neutrals collide intensively with the surrounding solid walls. However, in the areas to the right and left of the divertor the temperature remains high and in all cases above 500 K. It is also clearly demonstrated that the increase in the pumping probability always increases the temperature in the area above the pumping opening. This last observation is in line with the aforementioned comments on the

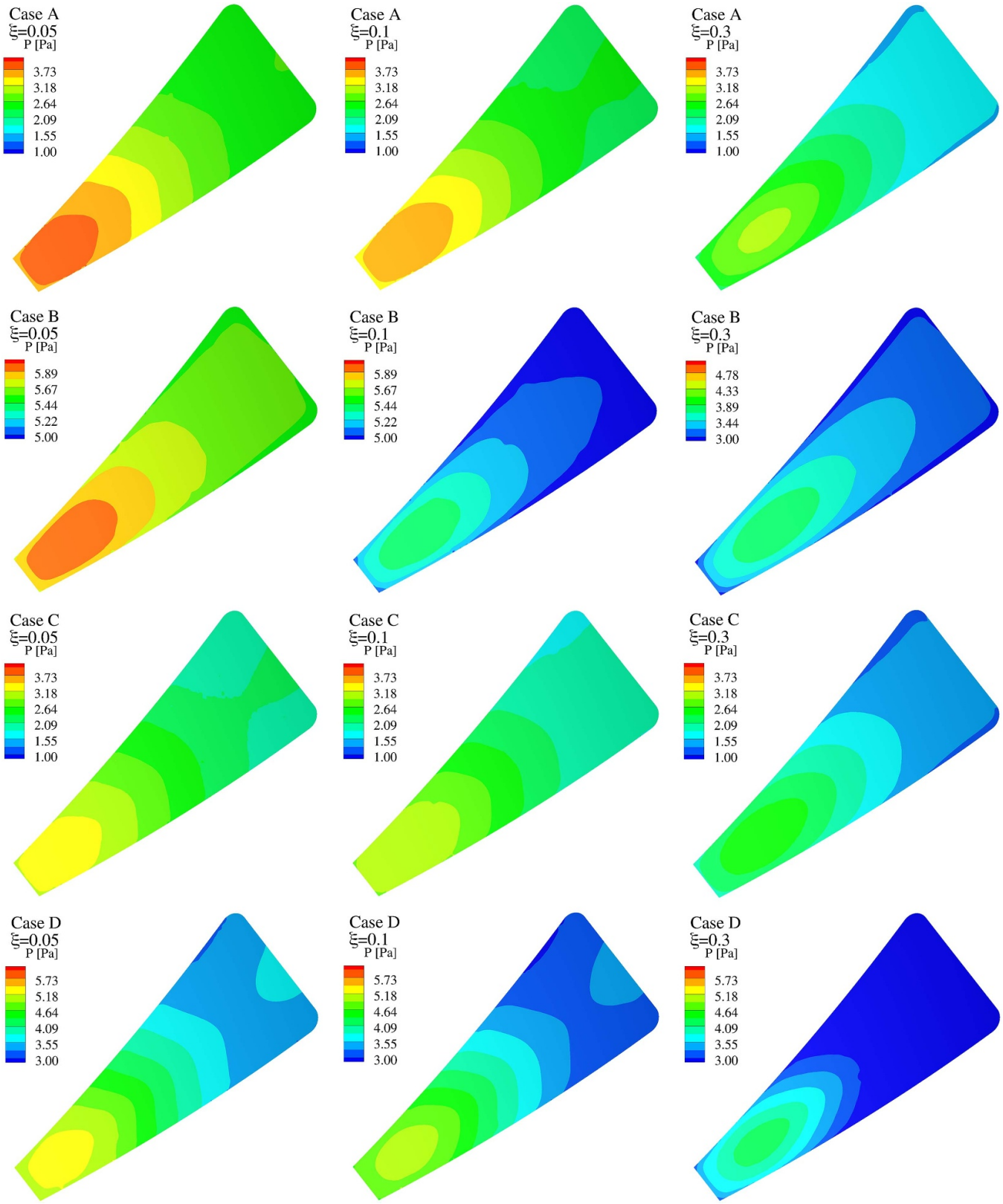

Figure 8. Overall pressure contours at the pumping opening for the cases A, B, C, and D and for various values of ξ.

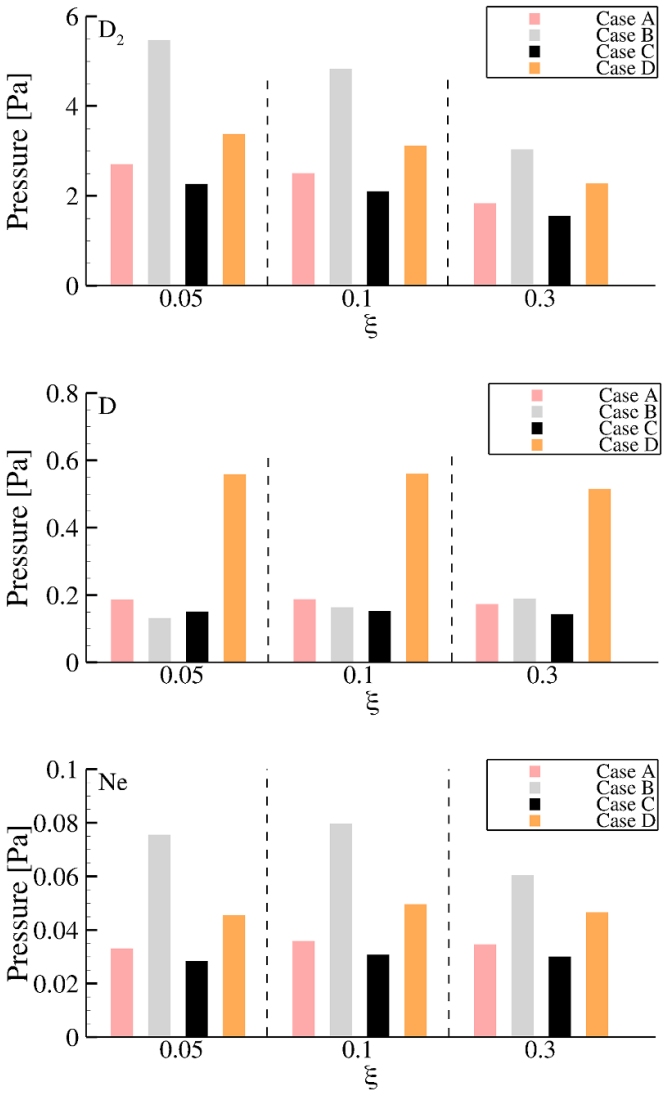

Figure 9. Average partial pressures of molecular deuterium (top), atomic deuterium (middle) and neon (bottom) at the pumping opening for various values of ξ.

temperature contours across the pumping opening presented in figure 10.

4.3. Pumping speed

As it is shown in the previous subsections, varying the pumping probability ξ provides a unique opportunity to investigate parametrically the neutral gas dynamics inside the subdivertor area and to compare the various examined cases on the same basis (i.e. the same pumping probability). The role of introducing a variable pumping probability ξ is to decouple the divertor particle exhaust behaviour from the technological solution of the vacuum pumping system. In practice, in order to assess the pumping efficiency of the divertor and to determine the pumping requirements it is important to know the relation between the pumping probability ξ and the effective pumping speed, both defined at the pumping opening. This information can be extracted with the present simulations and is given in figure 15, in which the function $S_\mathrm{p}(\xi)$ is plotted for the cases A–D. It is noted that the effective pumping speed S_p has been calculated as follows:

$$S_\mathrm{p}(\xi) = \frac{\Phi_\mathrm{pumped}(\xi)}{\bar{n}(\xi)}, \tag{4}$$

where, Φ_pumped is the pumped flux (per pumping opening) and $\bar{n}$ is the average number density across the pumping opening. The results indicate that the pumping speed S_p per pumping opening can be considered fairly (within 10% accuracy) as a linear function of ξ, with the deuterium pumping speed being always higher than the neon one by a factor of about 2.3. It has to be noted, however, that the cryopump system currently envisaged to be installed at DTT, is linked with different capture coefficients for heavy and light species, so that the apparent pumping speed difference is partly compensated. With respect to the different cases A–D, a small variation in pumping speed is observed, with the results for case D coming out slightly higher compared to the others. Overall, for $0.05 \leqslant \xi \leqslant 0.3$, the pumping speed per pumping opening for

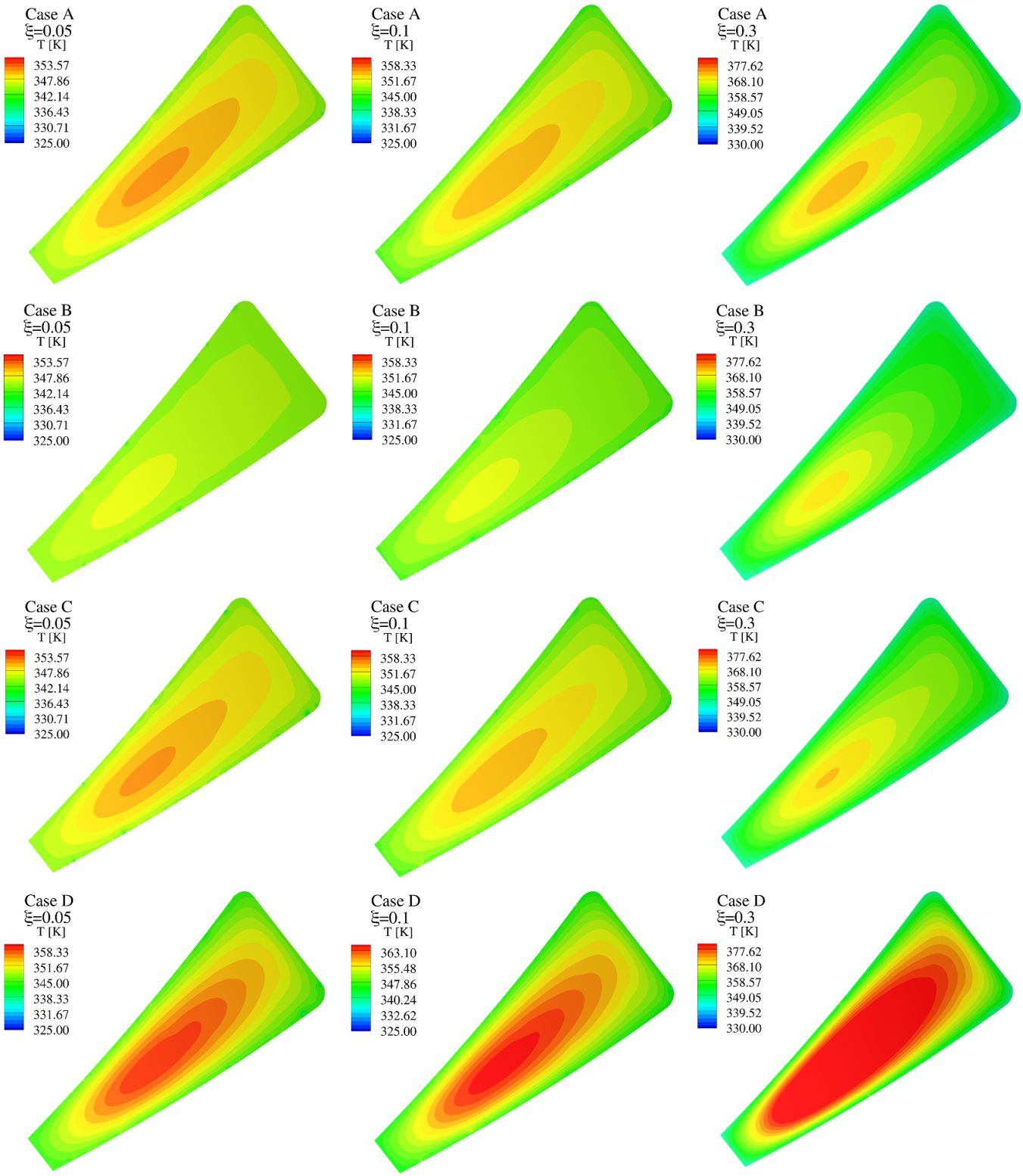

Figure 10. Overall temperature contours at the pumping opening for the cases A, B, C, and D and for various values of ξ.

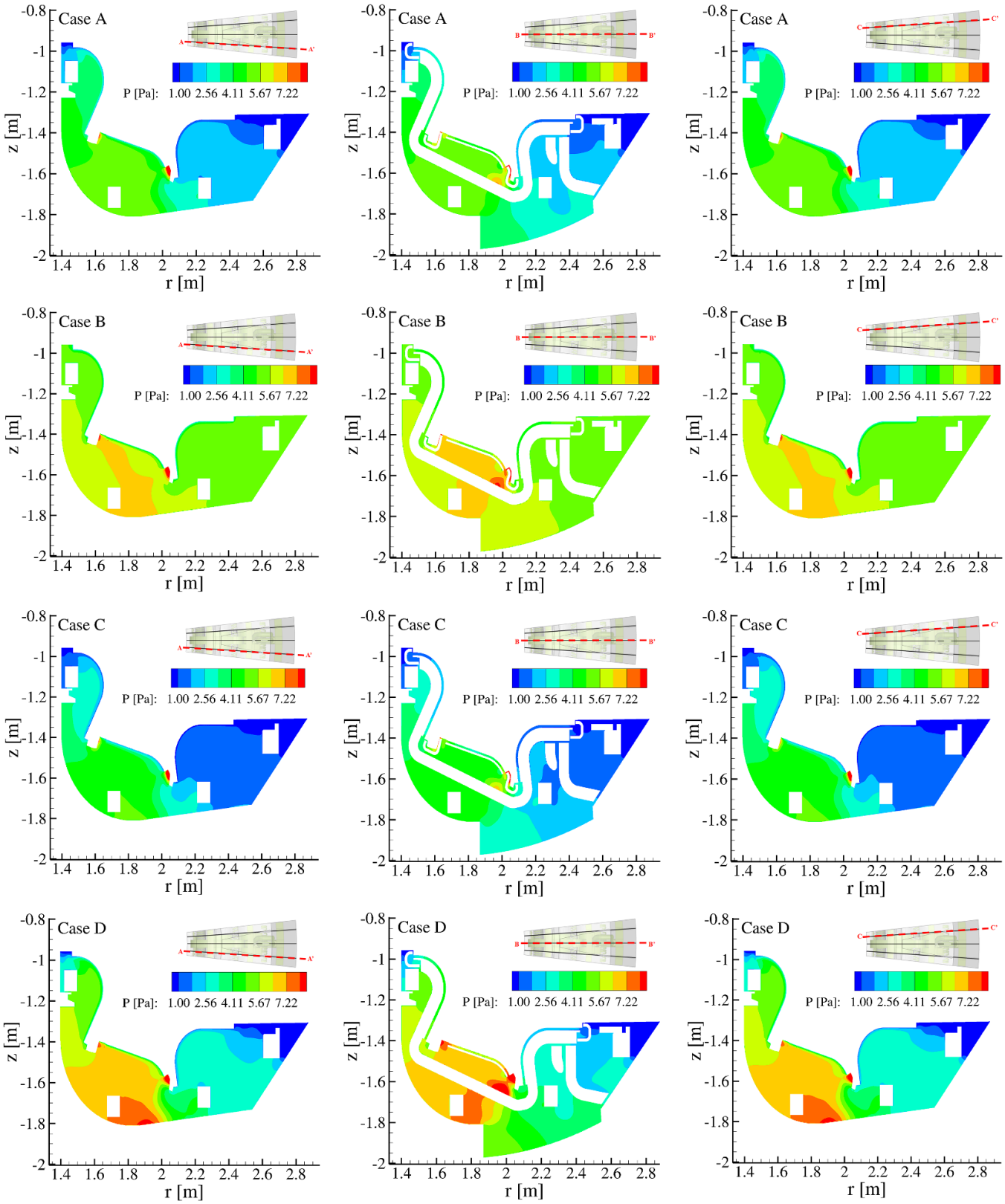

Figure 11. Overall pressure contours at different vertical cross sections for the cases A, B, C, and D and for $\xi = 0.05$.

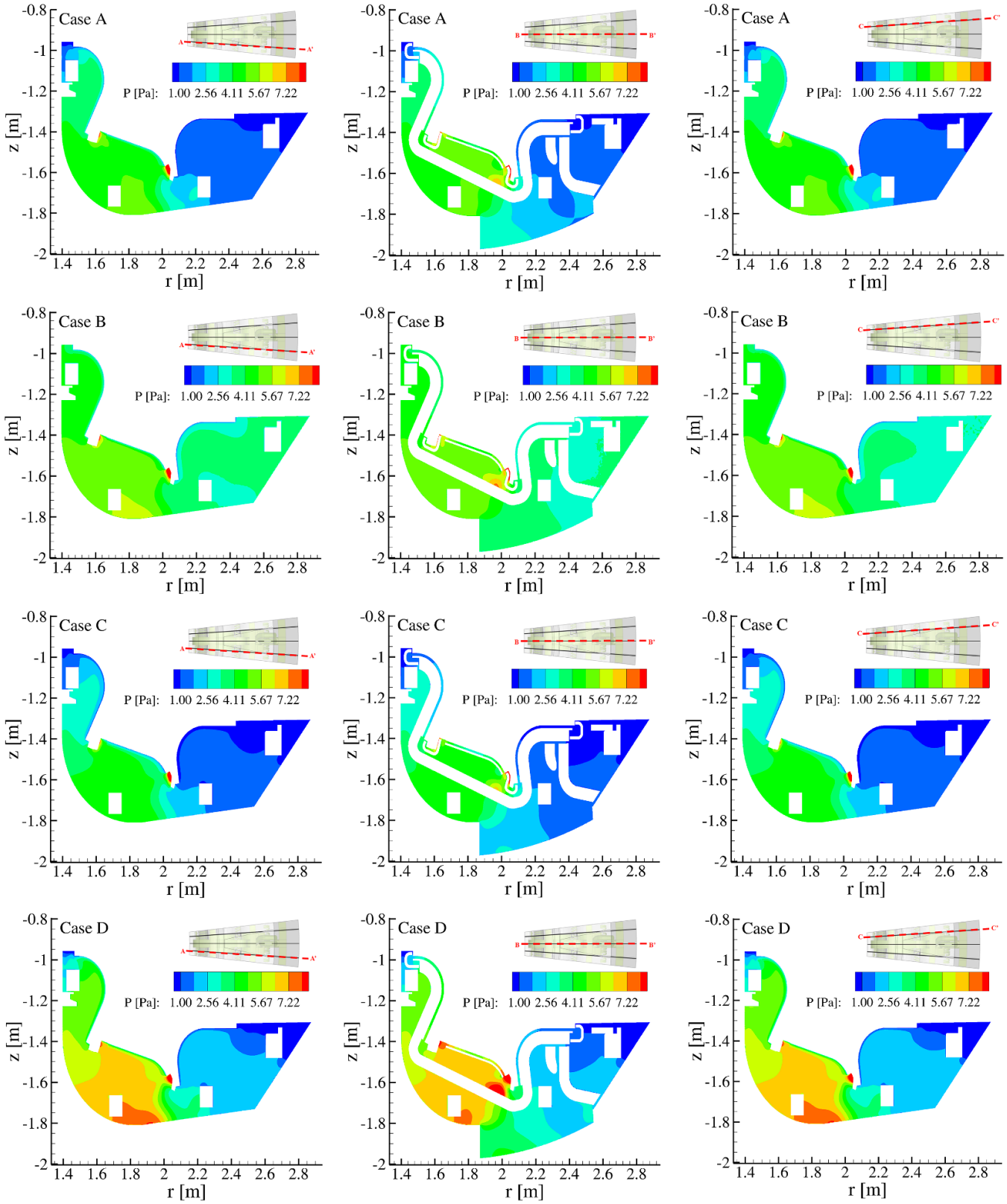

Figure 12. Overall pressure contours at different vertical cross sections for the cases A, B, C, and D and for $\xi = 0.3$.

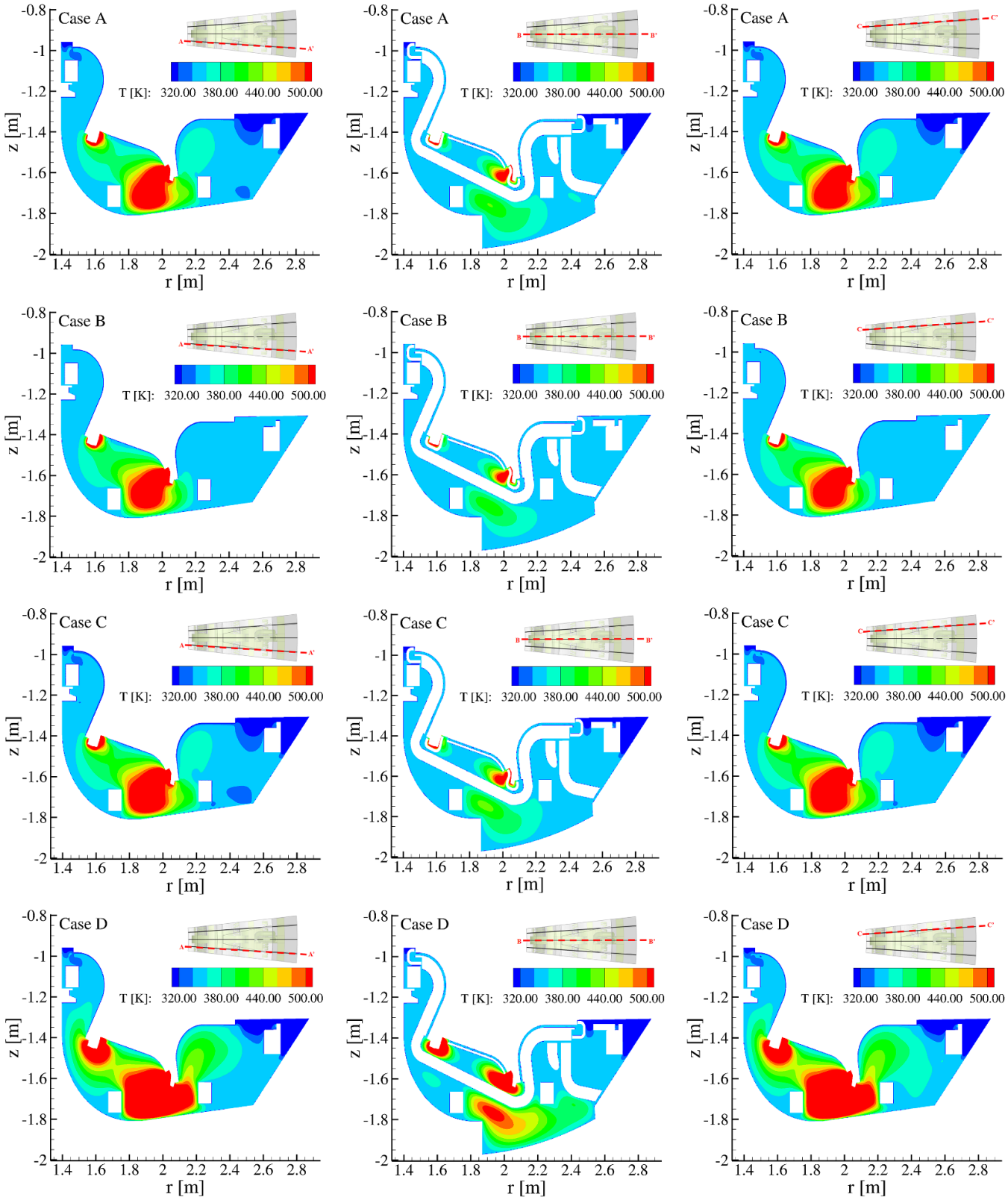

Figure 13. Overall temperature contours at different vertical cross sections for the cases A, B, C, and D and for $\xi = 0.05$.

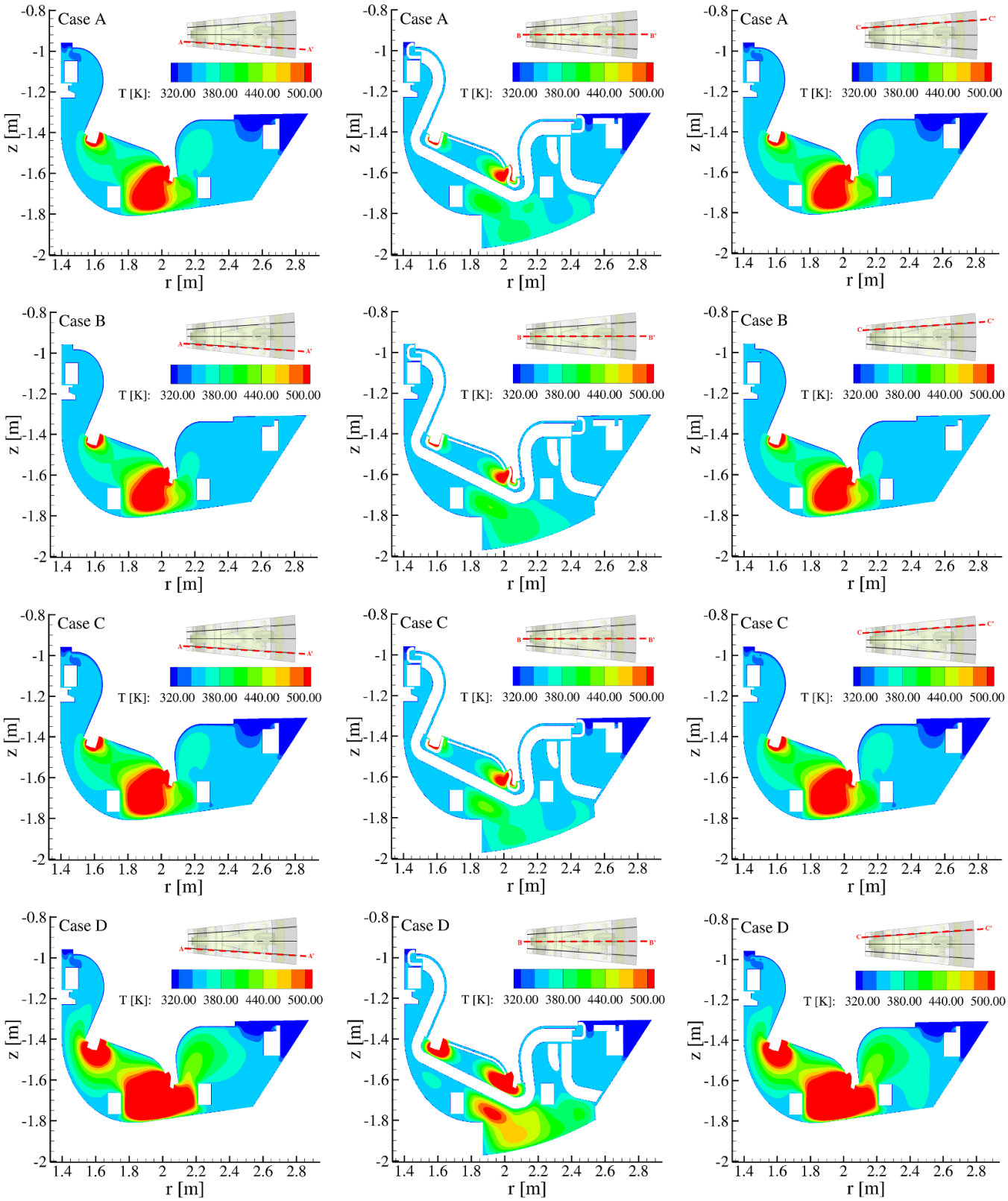

Figure 14. Overall temperature contours at different vertical cross sections for the cases A, B, C, and D and for $\xi = 0.3$.

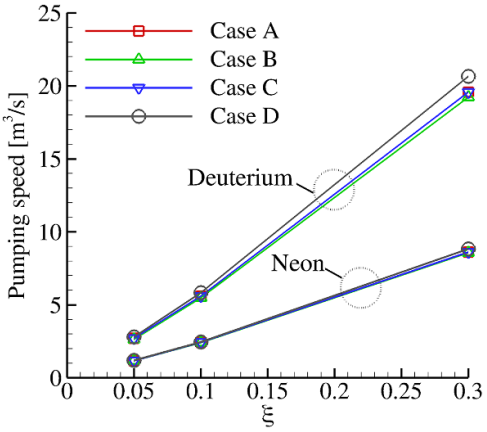

Figure 15. Pumping speed S_p [m^3 s^{-1}] per pumping opening vs. pumping probability ξ in the case of deuterium and neon and for the cases A, B, C, and D.

deuterium and neon is obtained as $2.7 \leqslant S_p \leqslant 21$ m^3 s^{-1} and $1.2 \leqslant S_p \leqslant 8.8$ m^3 s^{-1} respectively. It is noted that, the deuterium throughput for the same range of ξ varies between 8 and 40 Pa m^3 s^{-1}.

Based on the provided values for the pumping speed S_p per opening, it is interesting to study the relation between the overall flux over the whole divertor ring and the pumping speed per opening and thereby examine the different pumping requirements with respect to the cases A–D. In figure 16, the overall pumped flux for the whole divertor ring is plotted as a function of the pumping speed per opening, assuming different scenarios with respect to the number of available pumping openings in the toroidal direction. In this analysis, we assume that all the openings have the same pumping speed, and additionally, that the divertor ring pumped flux can be described simply as $\Phi_{\text{pumped}} \times$ No of openings. This assumption implies that the additional conductance effects coming from the divertor cassettes that are not centrally pumped are neglected, which seems to be justified on the basis of previous works on conductance modelling made for the ITER divertor [17]. In that way, the divertor ring pumped flux is believed to be somewhat overestimated with respect to the actual one, which could be obtained simulating the whole divertor ring, which even nowadays appears to be a task of tremendously high computational effort. In figure 16, the corresponding pumping requirements (defined by the imposed, i.e. $\Gamma_D = 8.4 \times 10^{22}$ D s^{-1} and $\Gamma_{Ne} = 1 \times 10^{21}$ Ne s^{-1}, see table 1) for deuterium and neon are shown by the dashed lines. Under steady state conditions, for a given pumping speed per opening and a number of available pumping openings the overall particle balance, i.e. $\Gamma_{D/Ne} = \Phi_{\text{pumped,D+D}_2/Ne} \times$ No of openings, should be satisfied. The results show that for deuterium and base case A, using the maximum available number of openings (=18) a minimum pumping speed of 10 m^3 s^{-1} per opening is required to satisfy the overall particle balance, while for the cases B, C, and D, the corresponding minimum pumping speed is about 4 m^3 s^{-1}, 13 m^3 s^{-1} and 7 m^3 s^{-1}, respectively. On the other hand, if the attached pumping speed could be doubled (pumping speed of 20 m^3 s^{-1}), the minimum required number of openings to satisfy the pumping requirements for the cases A, B, C, and D is 10, 8, 14 and 8 respectively. The current state of the pumping system design aims at using half of the available openings for pumping, i.e. only 9–10 out of 18 openings. More specifically, the results for case A show that with only 10 openings available, the pumping speed per opening would have to be about 20 m^3 s^{-1} per opening, corresponding to a ξ of about 0.3 (see figure 15), which is clearly at the upper limit of what is technically feasible given the narrow port geometry with trapezoidal cross-section. But the results also show that, by completely eliminating toroidal leakages, or limiting them as much as possible (e.g. by installing closure baffles) and at the same time limiting the effect of the cooling pipes (e.g. by reducing the number of pipes), the current divertor can meet the aforementioned limiting requirements.

4.4. Effect of the incoming neutral flux

In section 4.3 above, we discussed the necessary number of ports to close the particle balance at given plasma scenario and for the four divertor cases. In the present section, we want to better understand the effect of the incoming particle flux on the divertor neutral quantities which allows for a first order estimation of the variations of the pumping efficiency with respect to the inlet conditions. It is important to emphasize that this is only done in order to develop a feeling for the sensitivity of the incoming flux boundary condition on our findings, as the plasma scenario has not been adapted. The calculations have been repeated for a hypothetical incoming flux $\Phi_{\text{in,D/Ne}} = 0.65 \times \Phi^{\text{Table 1}}_{\text{in,D/Ne}}$ at otherwise unchanged conditions. Figure 17 compares the found results with the ones obtained for $\Phi_{\text{in,D/Ne}} = \Phi^{\text{Table 1}}_{\text{in,D/Ne}}$. Interestingly, the results show that for all examined cases A-D, a 35% decrease in the incoming flux causes the same decrease in the pumped flux. This implies that, at least for small variations of the incoming flux, the found pumping behaviour is characteristic for the divertor particle exhaust capability at the given plasma scenario. Regarding the effect of the incoming flux reduction on the subdivertor pressure, although the same qualitative behaviour has been observed as shown in figures 11–12, the pressure is affected only quantitatively. In figure 18, the average partial pressures of D, D_2, and Ne are shown for the cases A–D in the case of the hypothetical incoming flux of $\Phi_{\text{in,D/Ne}} = 0.65 \times \Phi^{\text{Table 1}}_{\text{in,D/Ne}}$. By comparing the pressure values in figure 18 with the corresponding ones in figure 9 for $\Phi_{\text{in,D/Ne}} = \Phi^{\text{Table 1}}_{\text{in,D/Ne}}$ and for the same value of ξ (i.e. same pumping speed), it is observed that a percentage decrease in the pumped flux about 35%, leads to a significant percentage decrease in the partial pressures about 55%–68%, 29%–32%, 32%–34% for D, D_2, and Ne, respectively.

We tried also to compare it quantitatively against experiments from AUG values in [18], in which the gas puff rate

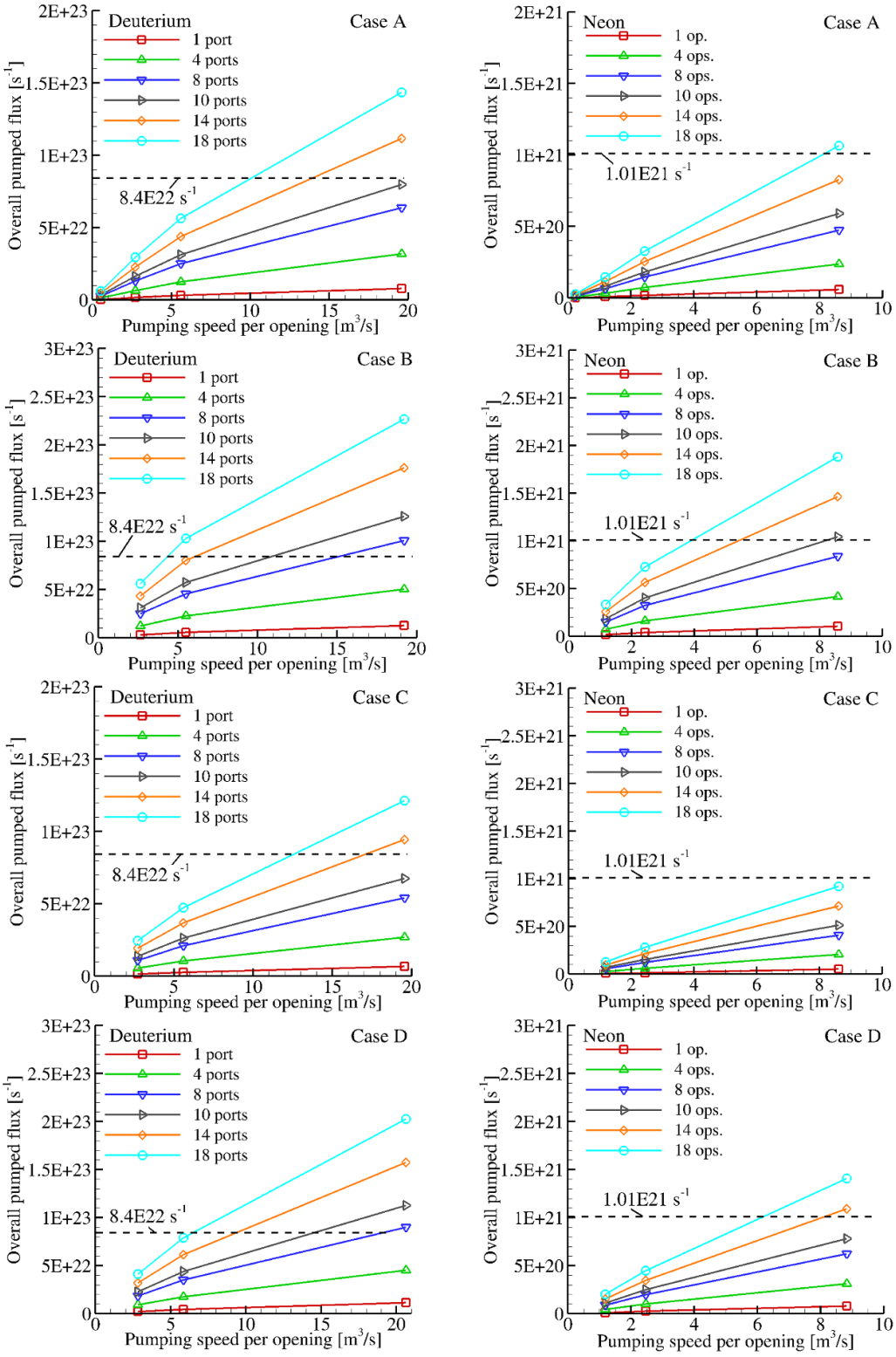

Figure 16. Overall pumped flux [s^{-1}] vs pumping speed per opening [m^3 s^{-1}] as a function of number of ports for deuterium (left) and neon (right) and for cases A, B, C and D. The target puffing fluxes are shown by dashed lines.

varied and the divertor pressure was measured at different connected pumping speeds. In [18], the experimental measurements in AUG show that in equilibrium the subdivertor neutral pressure is proportional to the gas puff rate for a given pumping speed. In order to assess whether the present results follow the aforementioned qualitative behaviour of the experimental measurements in [18], in figure 19, the present numerical data for the pressure at the pumping opening are plotted as a function of the overall pumped flux considering the cases $\Phi_{\mathrm{in,D/Ne}} = 0.65 \times \Phi^{\mathrm{Table\ 1}}_{\mathrm{in,D/Ne}}$ and $\Phi_{\mathrm{in,D/Ne}} = \Phi^{\mathrm{Table\ 1}}_{\mathrm{in,D/Ne}}$. The

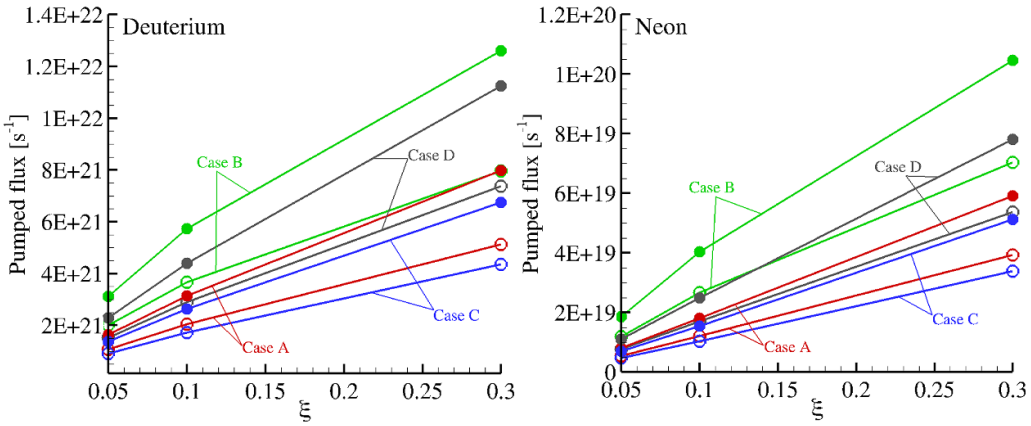

Figure 17. Pumped fluxes per opening for deuterium (left) and neon (right) vs ξ in the case of $\Phi_{\text{in,D/Ne}} = \Phi^{\text{Table 1}}_{\text{in,D/Ne}}$ (filled symbols) and $\Phi_{\text{in,D/Ne}} = 0.65 \times \Phi^{\text{Table 1}}_{\text{in,D/Ne}}$ (empty symbols).

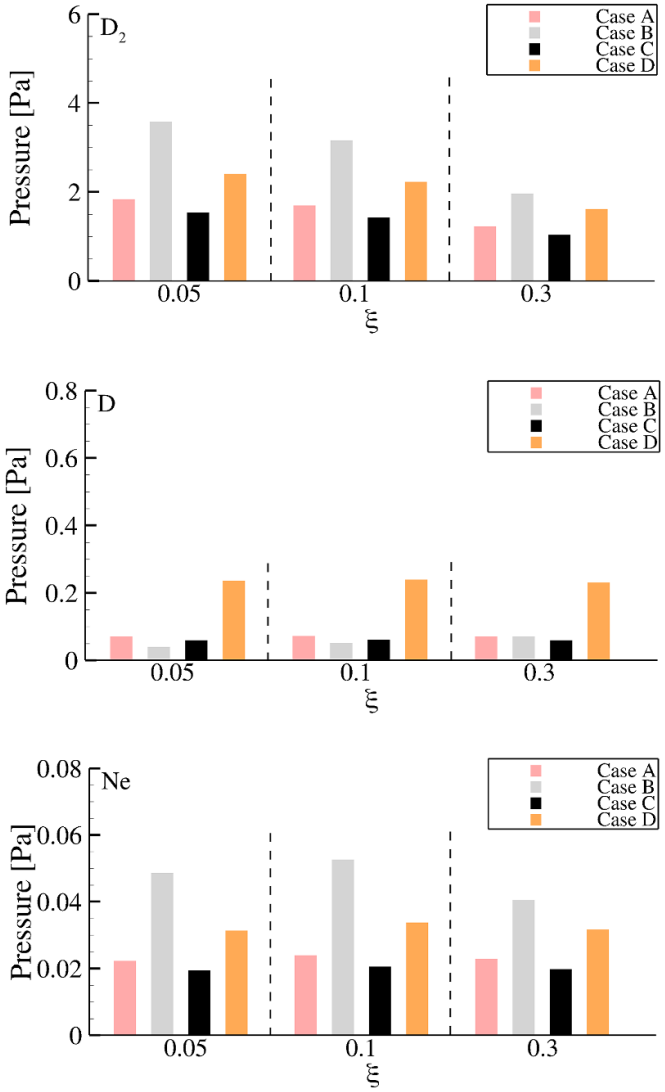

Figure 18. Average partial pressures of molecular deuterium (top), atomic deuterium (middle) and neon (bottom), at the pumping opening for various values of ξ in the case of an hypothetical incoming flux $\Phi_{\text{in,D/Ne}} = 0.65 \times \Phi^{\text{Table 1}}_{\text{in,D/Ne}}$.

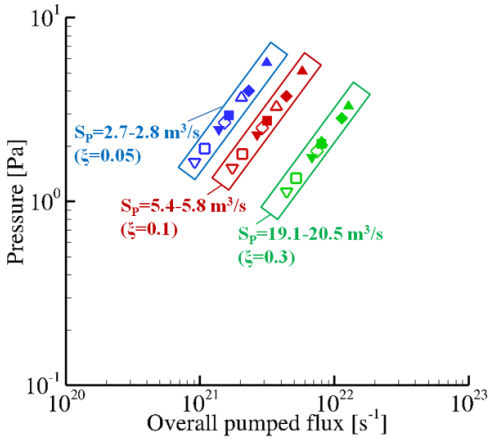

Figure 19. Average overall mixture pressure at the pumping opening vs overall net pumped flux per pumping opening. Data for $\Phi_{\text{in,D/Ne}} = \Phi^{\text{Table 1}}_{\text{in,D/Ne}}$ and $\Phi_{\text{in,D/Ne}} = 0.65 \times \Phi^{\text{Table 1}}_{\text{in,D/Ne}}$ are shown with the filled and empty symbols respectively. The results for the cases A, B, C, D are shown with squares, triangles, gradients and diamonds respectively.

results for all the cases A, B, C and D are grouped according to the values of the pumping probability ξ (or pumping speed). As it can be seen, the present numerical data reproduce the qualitative picture extracted from the AUG experiments and confirm the linear relationship between the pressure at the pumping opening and the pumped flux. The pumping speed always stands as the constant of proportionality in the relationship of the number density and the pumped flux.

5. Concluding remarks

In the present work, a systematic study of the pumping performance of the latest DTT divertor design is carried out assuming various pumping scenarios with respect to the pumping probability. In this framework, the 3D simulation model covered a sector with all the internal structures, namely magnetic coils, cooling pipes, divertor cassette and supporting structures. The choice of the model was made, on the one hand, to balance the significantly increased computational needs of a three-dimensional analysis, but also to allow the systematic study of various three-dimensional effects that cannot be described by the corresponding two-dimensional approach. The base case in which all the toroidal and poloidal leakages are taken into account was defined. Three additional cases have been considered in order to investigate the influence of the size of the poloidal gaps, the permeability of the toroidal gaps by the neutrals, as well as the influence of the cooling pipes on the neutral gas flow. SolEdge2D-EIRENE deuterium plasma simulations at the maximum additional power in partially detached condition achieved by neon impurity seeding have been used and the corresponding boundary conditions for the present simulations of the subdivertor area have been extracted.

Scrutinizing the obtained numerical results, the most important conclusions can be summarized as follows:

- The analysis showed that the cooling pipes underneath the entry gaps reduce the pumping efficiency causing a decrease in the pumped flux about 24%–30%.
- The toroidal leakages affect significantly the pumping performance of the divertor causing a significant decrease in the pumped flux about 37%–47% and 43%–56% for deuterium and neon respectively. Same percentages apply also for the pressure at the pumping opening.
- The neutral flux through poloidal leakages constitutes of about 12%–17% of the incoming flux. The analysis showed that enlarging the poloidal gaps by a factor of two causes a significant increase in the poloidal flux losses by a factor 1.7.
- The results show that using the maximum available number of openings (=18) a minimum pumping speed of 10 m^3 s^{-1} per opening is required to satisfy the pumping requirements, while assuming a pumping speed of 20 m^3 s^{-1} the minimum required number of openings is ten. To relax the pumping speed requirement which is not easy to meet for the given port geometry, one should close the toroidal leakages as much as possible. Limiting the effect of cooling tubes (e.g. by reducing the number of tubes) is also useful, but is understood to be more complex to implement.
- A sensitivity analysis on the incoming neutral flux at unchanged plasma conditions showed that a decrease in the incoming fluxes causes the same decrease in the pumped flux, and a quantitatively similar reduction in the partial pressures at the pumping opening. In addition, the decrease in the incoming fluxes affects only slightly the pumping speed. The numerical results were found to be consistent with the previous published experimental data in AUG.

Overall, this study provides a complete overview of the pumping performance of the current DTT design and reveals potential limitations from the neutral pumping point of view. It is noted that, the obtained results provide quantitative and qualitative indication of the pumping divertor performance for a reference plasma scenario. This paper shows the level of divertor complexity that can be adopted in the numerical modeling and the type of conclusions that can be drawn based on such studies.

Acknowledgments

This work has been carried out within the framework of the EUROfusion Consortium, funded by the European Union via the Euratom Research and Training Programme (Grant Agreement No 101052200—EUROfusion). Views and opinions expressed are however those of the author(s) only and do not necessarily reflect those of the European Union or the European Commission. Neither the European Union nor the European Commission can be held responsible for them. In addition, this work was performed within the 7$^{\text{h}}$ cycle of MARCONI-FUSION HPC (Project TOK-KIT) and also partially on the HoreKa supercomputer (Project ngdsim) funded by the Ministry of Science, Research and the Arts Baden-Württemberg and by the Federal Ministry of Education and

Research. Moreover, we acknowledge support by the KIT-Publication Fund of the Karlsruhe Institute of Technology.

ORCID iDs

C. Tantos https://orcid.org/0000-0003-1382-2364
S. Varoutis https://orcid.org/0000-0002-7346-9569
P. Innocente https://orcid.org/0000-0001-8726-994X

References

[1] ENEA 2015 DTT-divertor tokamak test facility. Project proposal *DTT "Blue Book"* (ENEA) (available at: www.dtt-project.it/) (Accessed 7 February 2022)
[2] ENEA 2019 DTT-divertor tokamak test facility, interim design report *DTT "Green Book"* (ENEA) (available at: www.dtt-project.it/) (Accessed 7 February 2022)
[3] Bird G.A. 1963 Approach to translational equilibrium in a rigid sphere gas *Phys. Fluids* **6** 1518–9
[4] Bird G.A. 1970 Direct simulation and the Boltzmann equation *Phys. Fluids.* **13** 2676–81
[5] Wagner W. 1992 A convergence proof for Bird's direct simulation Monte Carlo method for the Boltzmann equation *J. Stat. Phys.* **66** 1011–44
[6] Gleason-González C., Varoutis S., Luo X., Shimizu K., Nakano T., Hoshino K., Kawashima H., Asakura N., Day C. and Sakura S. 2016 Simulation of collisional effects on divertor pumping in JT-60SA *Fusion Eng. Des.* **109–111** 693–9
[7] Varoutis S., Gleason-González C., Moulton D., Kruezi U., Groth M., Day C., Wiesen S. and Harting D. (JET Contributors) 2017 Simulation of neutral gas flow in the JET sub-divertor *Fusion Eng. Des.* **121** 13–21
[8] Bonelli F., Varoutis S., Coster D., Day C. and Zanino R. (JET Contributors) 2017 Self-consistent coupling of DSMC method and SOLPS code for modeling tokamak particle exhaust *Nucl. Fusion* **57** 066037
[9] Varoutis S., Igitkhanov Y. and Day C. 2019 Assessment of the 3D geometrical effects on the DEMO divertor pumping efficiency *Nucl. Mater. Energy* **19** 120–3
[10] Tantos C., Varoutis S. and Day C. 2020 Deterministic and stochastic modeling of rarefied gas flows in fusion particle exhaust systems *J. Vac. Sci. Technol.* B **38** 064201
[11] Tantos C., Varoutis S., Day C., Balbinot L., Innocente P. and Maviglia F. 2022 DSMC simulations of neutral gas flow in the DTT particle exhaust system *Nucl. Fusion* **62** 026038
[12] Borodin D.V.*et al* 2022 Fluid, kinetic and hybrid approaches for neutral and trace ion edge transport modelling in fusion devices *Nucl. Fusion* **62** 086051
[13] Shen C. 2005 *Rarefied Gas Dynamics: Fundamentals, Simulations and Micro Flows* (Springer)
[14] Assael M.J., Mixafendi S. and Wakeham W.A. 1987 The viscosity of normal deuterium in the limit of zero density *J. Phys. Chem. Ref. Data* **16** 189–92
[15] Stallcop J.R., Levin E. and Partridge H. 1998 Transport properties of hydrogen *J. Thermophys. Heat Transfer* **12** 514–9
[16] Borgnakke C. and Larsen P.S. 1975 Statistical collision model for Monte Carlo simulation of polyatomic gas mixture *J. Comput. Phys.* **18** 405–20
[17] Hauer V. and Day C. 2015 ITER divertor gas flow modelling *Fusion Eng. Des.* **98–99** 1775–8
[18] Kallenbach A., Sun H.J., Eich T., Carralero D., Hobirk J., Scarabosio A. and Siccinio M. (ASDEX upgrade team and EUROfusion MST1 team) 2018 Parameter dependences of the separatrix density in nitrogen seeded ASDEX upgrade H-mode discharges *Plasma Phys. Control. Fusion* **60** 045006